PHASE 1 UPGRADE OF THE HADRONIC FORWARD CALORIMETER – TESTING THE FRONTEND DAQ ELECTRONICS CARDS

by

Ohannes Kamer Köseyan

B.S., Physics, Yeditepe University, 2011

Submitted to the Institute for Graduate Studies in
Science and Engineering in partial fulfillment of
the requirements for the degree of
Master of Science

Graduate Program in Physics

Boğaziçi University

2016

ACKNOWLEDGEMENTS

I am heartily thankful to my supervisor Erhan Gülmez, for his great support, guidance and patience.

I am also thankful to my family and friends for their support and patience.

ABSTRACT

PHASE 1 UPGRADE OF THE HADRONIC FORWARD CALORIMETER – TESTING THE FRONTEND DAQ ELECTRONICS CARDS

The original CMS HF Photomultiplier tubes (PMT) that were used by the CMS experiment during Run I were Hamamatsu R7525 single anode PMTs. These PMTs had a known issue of producing anomalous events due to the Cherenkov radiation produced by the muons passing through their thick front windows. In the first part of the phase 1 upgrade of the HF detector, these PMTs were replaced with Hamamatsu R7600U-200-M4, which was a 4-anode PMT with a thinner front window, to deal with this problem. This model was selected, because its thinner front window would reduce the amount of Cherenkov radiation and having multiple anodes would provide one more distinction between normal events and window events. The new thinner window significantly reduced the amount of Cherenkov radiation, but did not eliminate it completely. However, due to the lack of enough input channels on the frontend DAQ system of the HF, the new PMTs were connected as if they were single anode PMTs. The second part of this upgrade is the replacement of the frontend DAQ system with the new one that has more input channels, in order to make it possible to connect these new PMTs as if they were 2-anode PMTs. After the second part of the phase 1 upgrade, it will be possible to eliminate more of these window events via additional information coming from two pairs of anodes of these new PMTs. The new DAQ system will also have a time-to-digital converter (TDC) functionality to track the timing of the events, which will help this elimination further. As part of this thesis, 180 DAQ cards were tested.

ÖZET

İLERİ HADRON KALORİMETRESİ 1. AŞAMA GÜNCELLEME ÇALIŞMALARI - ÖN UÇ VERİ ALIM ELEKTRONİK KARTLARININ TESTİ

CMS deneyinin İleri Hadron Kalorimetresi tarafından Run I döneminde kullanılan orijinal fotoçoğaltıcı tüpleri (PMT), tek anotlu olan Hamamatsu R7525 modeliydi. Bu PMTlerde, gelen müonların tübün ön penceresinde yaptığı Çerenkov ışıması sebebiyle beklenmedik sinyallerin oluşması bilinen bir sorundu. HF kalorimetresinin 1. aşama güncelleme çalışmalarının ilk kısmında, bahsi geçen sorunun çözümü olarak bu PMT'ler 4 anotlu ve eski PMT'lerden daha ince bir ön pencereye sahip olan Hamamatsu R7600U-200-M4 modeliyle değiştirildi. Bu modelin seçilmesinin sebebi, ön pencerelerinin daha ince olması sayesinde Çerenkov ışınımının azalacağı ve birden fazla anoda sahip olmanın bu beklenmedik olayların daha kolay ayırt edilmesini sağlayacağıydı. İnce ön pencereler, Çerenkov ışınımını önemli ölçüde azalttı, ancak tamamen ortadan kaldıramadı. Ayrıca, ön uç veri alım sisteminde yeterli sayıda giriş kanalının olmaması sebebiyle bu yeni 4 anotlu PMT'ler, tek anotluymuş gibi kullanıldı. 1. aşama güncelleme çalışmalarının ikinci kısmı ise, HF'in veri alım elektroniklerinin yenisiyle değiştirilmesi suretiyle giriş kanalı sayısının artırılması ve yeni PMT'lerin 2 anotlu olarak kullanılacak şekilde bu sisteme bağlanması işleridir. Bu işlerin sonucunda hatalı sinyallerin ayıklanması daha iyi yapılabilecektir. Yeni veri alım sisteminde, PMT sinyallerinin zamanlamasını yapacak olan zaman-sayısal çevirici (TDC) özelliği de bulunacaktır. Bu özellik, veri alım sisteminin hatalı sinyal ayıklama işine yardımcı olacaktır. Bu tezin bir parçası olarak, 180 adet veri alım kartı test edildi.

TABLE OF CONTENTS

LIST OF FIGURES

LIST OF TABLES

LIST OF SYMBOLS

fC	Femto Coulomb
Gbps	Gigabit per second
GeV	Giga electron-volt
K	Kelvin
MeV	Mega electron-volt
MHz	Megahertz
Q	Charge
T	Tesla
TeV	Tera electron-volt
η	Pseudorapidity
ϕ	Azimuthal angle
$\mathcal{L}$	Luminosity

LIST OF ACRONYMS/ABBREVIATIONS

ADC	Analog to Digital Converter
ALICE	A Large Ion Collider Experiment
ATLAS	A Toroidal LHC ApparatuS
BE	Backend
BGA	Ball Grid Array
CM	Centre of Mass
CMS	Compact Muon Solenoid
DAQ	Data Acquisition
EB	Electromagnetic Barrel
ECAL	Electromagnetic Calorimeter
EE	Electromagnetic Endcap
FE	Frontend
FPGA	Field Programmable Gate Array
HB	Hadron Barrel Calorimeter
HE	Hadron Endcap Calorimeter
HF	Hadron Forward Calorimeter
HO	Hadron Outer Calorimeter
HCAL	Hadron Calorimeter
HPD	Hybrid Photodiode
IP	Interaction Point
LEP	Large Electron-Positron Collider
LHC	Large Hadron Collider
LHCb	LHC Beauty
ngCCM	New Generation Clock and Control Module
PCB	Printed Circuit Board
PMT	Photomultiplier Tube
PS	Proton Synchrotron
PSB	Proton Synchrotron Booster

QIE	Charge Integrator and Enumerator
RF	Radio Frequency
ROBOX	Readout box
SMT	Surface Mount Technology
SPS	Super Proton Synchrotron
TDC	Time to Digital Converter
μHTR	Micro HCAL Trigger Readout
UXC	CMS Cavern
VTTx	Versatile Twin Transmitter

1. INTRODUCTION

The Large Hadron Collider is the world's largest particle accelerator and collider. It is designed and built to accelerate the protons up to an energy of 7 TeV with a center of mass energy of 14 TeV for the collisions and a luminosity of $\mathcal{L} = 10^{34} m^{-2} s^{-1}$. It is built as a discovery machine to find and study various kinds of particles. It was the machine in which the famous Higgs Boson was discovered.

The Compact Muon Solenoid (CMS) is one of the two main general purpose particle detector experiments that is housed in the LHC, which allows scientists to study various physical phenomena via analyzing the collision data.

Hadron Forward (HF) Calorimeter is an important part of the CMS detector that detects the particles within the pseudorapidity range of $3 < |\eta| < 5$. It is a sampling calorimeter that uses steel as an absorber material and quartz fibers as the active elements. Particle showers created in the absorbers produce Cherenkov radiation as they pass through the quartz fibers.

During Run I, Hamamatsu R7525 single anode PMTs were used in the HF. A known issue with those PMTs was that their thick front windows were getting hit by muons and producing anomalous signals via Cherenkov radiation. In the first part of the Phase 1 upgrade, these PMTs were replaced with Hamamatsu R7600U-200-M4 PMTs to solve this issue. These PMTs have 4 anodes and a thinner window. The goal of this upgrade was to reduce the rate of the Cherenkov radiation production at the PMT windows by having thinner windows. Also, having multiple anodes on each PMT allowed the possibility to distinguish more of these anomalous signals from the real ones. But the Data Acquisition (DAQ) Frontend (FE) system didn't have enough channels to read all four anodes of each PMT separately. Thus, the four channels of each PMT were ganged together and connected to one DAQ channel, as if it were a single anode PMT. Also the DAQ system didn't have a TDC to track the timing of the events.

The goal of the second part of the Phase 1 upgrade is to replace the DAQ system to have more channels, so that each PMT can be connected to two DAQ channels, as if it were a 2-anode PMT. Also the new DAQ system will incorporate a TDC functionality to track the timing of the events.

The main subject of this thesis is the upgrade of the HF FE DAQ electronic cards. The first chapters will cover the information about the LHC, the CMS experiment, the Hadronic Calorimeter (HCAL) and the Hadron Forward (HF) Calorimeter. Later chapters will briefly cover the HF PMT upgrade, the components of the new DAQ system, FE DAQ system upgrade, production of the electronic cards and the results of the tests done on them.

2. LARGE HADRON COLLIDER

The Large Hadron Collider (LHC) is the world's largest and most energetic particle collider, located between France and Switzerland, near Geneva. It is a proton synchrotron that has a circumference of 27 km and lies inside a tunnel, which is approximately 100 m underground. LHC was built into a tunnel, which previously housed the Large Electron – Positron Collider (LEP) experiment. LEP was the previous collider at CERN and was built into this 100 m deep tunnel, because it was less costly to build such tunnel than to acquire the land above the ground. Also, the natural rock around the tunnel helps for shielding the radiation coming from the outside environment, since it may interfere with the detectors. It also shields the environment from vast amounts of extremely energetic radiation that is being created by the collider. Since building another tunnel for the LHC would be vastly expensive, the same tunnel was used.

The LHC contains each of its proton beams inside a pair of beam pipes. These beams travel in opposite directions inside each of the beam pipes and are set to collide at the designated interaction points. These points are at the center of each one of the four big experiments. To keep the protons in orbit around the accelerator, 1232 superconducting dipole magnets are used. Each of these dipoles has a length of 14.3 m. 392 superconducting quadruple magnets are also placed around the accelerator to keep the beam focused throughout the collider. Sextupole, octopole and decapole magnets are also used to fine tune the focusing of the beams. These superconducting magnets are constructed from niobium-titanium wires and are cooled by liquid helium down to 1.9 K. Liquid helium in the LHC is in a superfluid state. Superfluidity helps to cool the windings by seeping through each and every gap between and around the windings, leaving no uncooled part throughout the magnet. [1]

Protons in the LHC are accelerated by superconducting RF (radio frequency) cavities. RF cavities are basically electrically conductive resonant hollow structures that create oscillating electric and magnetic fields at a certain frequency. These cavities

act like LC tank circuits, thus the frequency of the fields created by them depend on the geometry and the electric and magnetic constants of the media where these fields are created. Protons are accelerated by the oscillating electric fields. RF cavities in the LHC are tuned to 400 MHz. The reason for these cavities being superconductive is to eliminate the loss of energy in the form of heat due to the electrical resistance of the cavity walls.

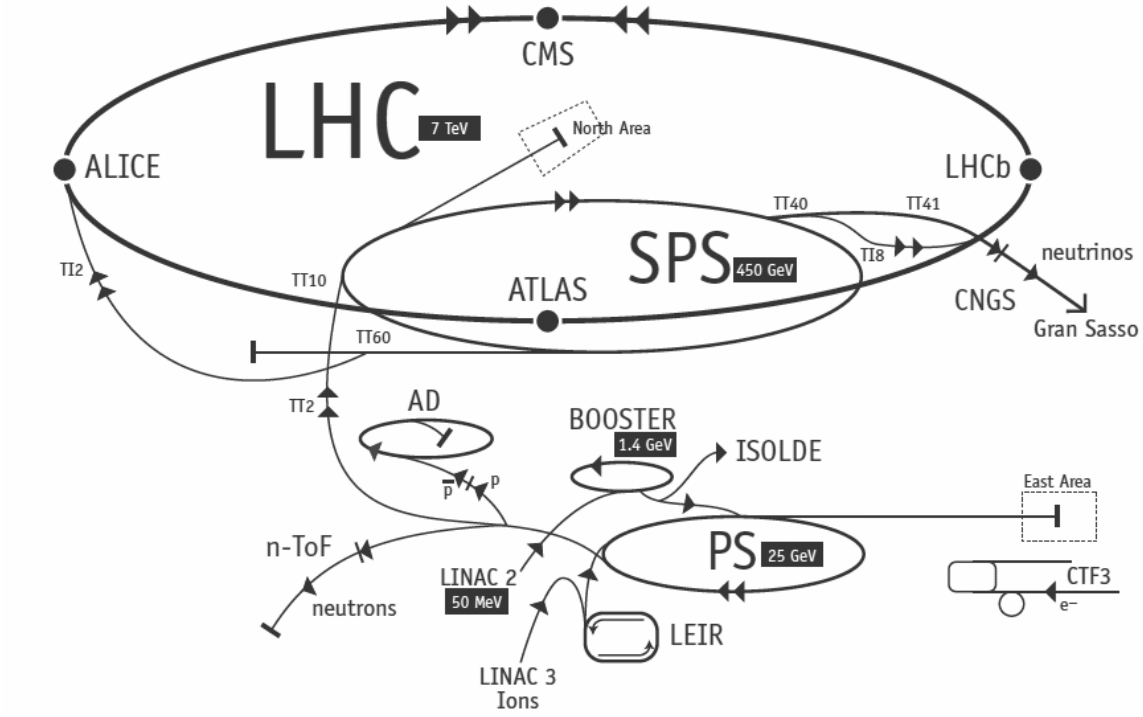

Figure 2.1. Diagram of the accelerators at CERN, including the LHC accelerator, its pre-accelerators and the other experiments. [2]

The LHC does not accelerate the protons from rest. There are a couple of accelerators before the LHC (Figure 2.1). First, protons are produced by ionizing gaseous hydrogen in a large electric field. Then, these protons are injected into Linac II. Linac II is the first acceleration stage of the LHC complex. Protons leave the Linac II with a kinetic energy of 50 MeV. Particles that exit the Linac II are then injected into the Proton Synchrotron Booster (PSB). There, the protons are accelerated up to 1.4 GeV.

Afterwards, they are injected into the Proton Synchrotron (PS). There, they reach 25 GeV. After the PS, the protons have a speed of $0.99c$ relative to the lab frame, thus they don't get significant speed increases anymore beyond that point. After the PS, they are injected into the Super Proton Synchrotron (SPS). There, they get up to 450 GeV before being injected into the LHC. From there, LHC takes on the acceleration of these protons up to the designated maximum energy of the LHC. To maintain the orbit of such an energetic beam, superconducting dipole magnets in the LHC start with a magnetic field of 0.54 T at 450 GeV of energy and as the energy of each beam ramps up to 6.5 TeV, the magnetic field ramps up to 7.7 T.

The LHC was designed to accelerate protons up to 7 TeV per proton with a luminosity of $\mathcal{L} = 10^{34}\ cm^{-2}s^{-1}$. However, due to some limitations during the first operational run, protons could only be accelerated up to 3.5 TeV at that time, which made the CM energy 7 TeV. In the last year of the Run I period, the CM energy was increased to 8 TeV. These limitations were fixed during the long shutdown between 2013 and 2015. Then (on March 2015), LHC was able to accelerate and maintain proton beams up to 13 TeV CM energy (6.5 TeV per beam).

There are four big experiments at the LHC, each one being around an interaction point. These four experiments are ATLAS, CMS, ALICE and LHCb. ATLAS and CMS are general-purpose detectors that have led to the discovery of the Higgs Boson. ALICE is a detector that is optimized for heavy ion collisions. It is one of the detectors that is used for the study of the quark-gluon plasma. And the last experiment, LHCb, is designed and optimized for the detection of b-physics events. B-physics events are such events that involve hadrons with one or more bottom quarks in them. This detector is used for the measurements regarding the CP violation. The potential results of this experiment may shed light to the explanation of the matter-antimatter asymmetry in our universe.

3. COMPACT MUON SOLENOID

CMS is one of the four big experiments on the LHC (Figure 3.1). It is 21.6 m long 15 m in diameter and weighs about 14000 tonnes. CMS is large not only in terms of its dimensions, but also in terms of the size of its collaboration. Having approximately 3500 people from 193 institutions in 43 countries, it is one of the largest scientific collaborations in the world. The detector is located at the northernmost part of the LHC, inside a cavern 100 m below Cessy, France. It was built as a general-purpose detector for the detection and the measurement of the energies and momenta of photons, electrons, hadrons and muons. Its main goals are to explore the physics in TeV scale, to discover and to analyze the properties of the Higgs Boson, to explore the physics beyond the Standard Model, such as supersymmetry, and to study the aspects of the heavy ion collisions. It was one of the two main detectors (the other one being ATLAS) that led to the discovery of the Higgs Boson. CMS consists of five main parts: Tracker, Electromagnetic Calorimeter (ECAL), Hadron Calorimeter (HCAL), superconducting solenoid magnet and muon chambers. [3]

3.1. Coordinate Conventions

The origin of the coordinate system of the CMS lies at the interaction point (IP) at the centre of the detector. Its +z axis lies on the cylindrical axis of the detector and points in the western direction, towards the Jura Mountains. The +x axis points towards the centre of the LHC and its +y axis points vertically upwards. The azimuthal angle ϕ is measured from the x axis and is on the x-y plane.

3.2. Rapidity and Pseudorapidity

Pseudorapidity is a widely used angular coordinate measure which is formulated as:

$$\eta = -\ln\left[\tan\left(\theta/2\right)\right] \tag{3.1}$$

where θ is the polar angle between the +z axis and the particle trajectory. The reason for η being used as a measure of angle is that the rapidity, which is the argument of a Lorentz boost tensor, is Lorentz invariant. Also, for very high longitudinal momentum values, the difference between polar angles are too small to deal with. Both rapidity and pseudorapidity diverge as the polar angle converges to either 0 or π. Another reason for its wide use is being that for very high forward momentum, rapidity and pseudorapidity converge to each other.

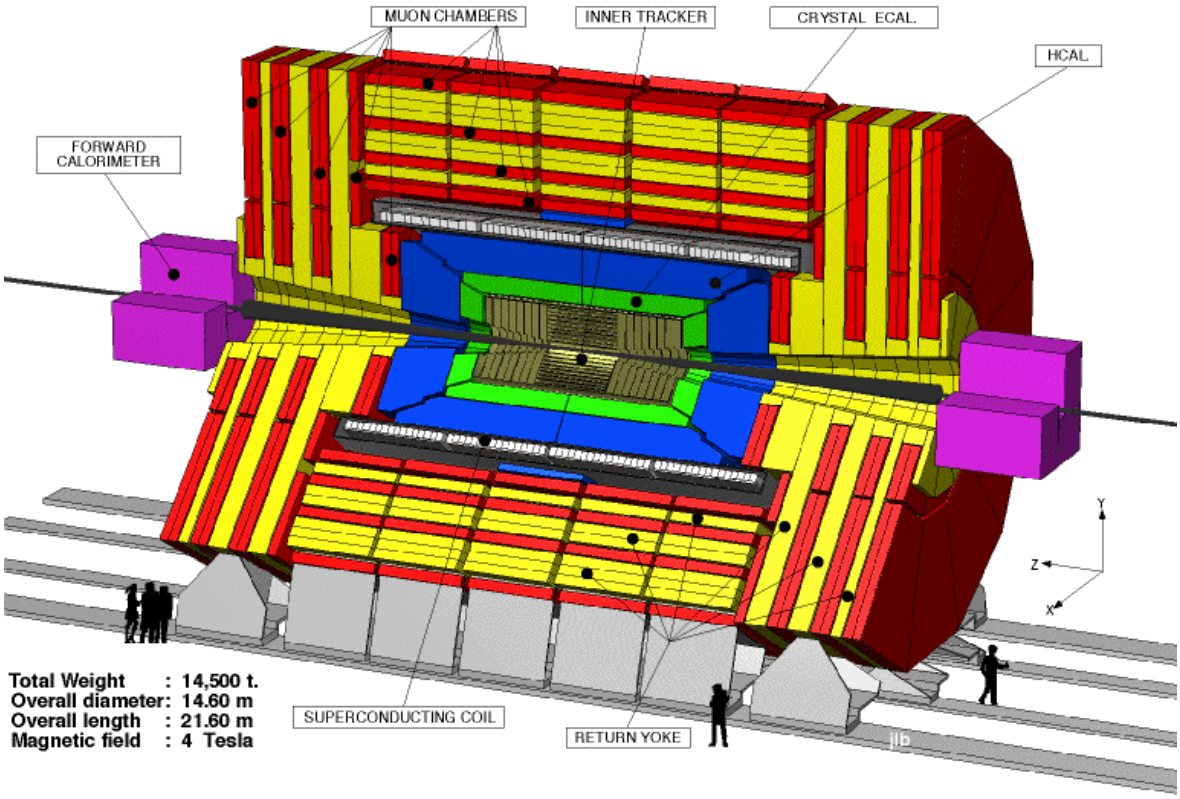

Figure 3.1. Cross section of the CMS along the axis of the beam pipe. [4]

3.3. Tracker

As seen in Figure 3.1, the innermost layer of the detector is the tracker. It consists of ten layers of silicon microstrip detectors and three layers of silicon pixel detectors as its cylindrical body. Also it has two endcaps with a total of 14 layers. It is used to

reconstruct the tracks and measure the times of flight of the charged particles resulting from the collisions. Paths of the particles are bent due to the magnetic field of the superconducting solenoid magnet. Time of flight and curvature information are used to infer the mass and the momentum of charged particles. This information is then used for particle recognition.

3.4. Electromagnetic Calorimeter

After passing through the tracker, the particles pass through the ECAL. Energies of the photons and charged leptons with low masses, namely electrons, are absorbed and measured here. Hadronic particles on the other hand, mostly pass through this subdetector without being affected much.

To measure the energies of these photons and electrons, lead tungstate scintillating crystals are used. One of the important properties of the Lead Tungstate crystals is that they are more sensitive to electrons and photons than hadrons. They also have a density of 8300 kg/m^3, which increases their probability to interact with these particles. Also, like all scintillators, they are transparent to visible light, despite their high mass density. The light created by these scintillators are then fed into and measured by the PMTs. Energy of the incident particle is proportional to the number of photons generated in scintillators per particle.

ECAL consists of two main parts, which are Electromagnetic Barrel (EB) and Electromagnetic Endcap (EE). Each of those consists of two halves (EE-, EE+, EB- and EB+), depending on their positions on the z-axis.

3.5. Hadron Calorimeter

After passing through ECAL, particles go into the Hadron Calorimeter (HCAL). Hadrons, either charged or neutral, are absorbed and get their energies measured in this detector. This detector will be discussed in detail in the next chapter.

3.6. Solenoid Magnet

Next layer is the superconducting solenoid magnet. The windings of this solenoid are made from a Niobium-Titanium alloy and are cooled down to 4.6 K, using superfluid liquid helium. The solenoid consists of 5 separate shorter solenoids and each of these solenoids draws 20000 Amperes of current. The strength of the magnetic field created by this solenoid is about 4 T. High magnetic field strength is required for better resolution for the momentum measurements done in the tracker and the muon system.

3.7. Muon System

Next layer, which is also the outermost layer of the CMS, is the muon system. It consists of strip wire chambers sandwiched together with iron return yokes. Strip wire chambers are used for detecting and reconstructing the tracks of muons and the iron return yokes are used for keeping the magnetic field in the solenoid and redirecting it to the muon system, for bending the paths of the muons. This magnetic field in the muon system is essential for the momentum measurement of the muons. This subdetector also consists of a barrel in the middle and a pair of endcaps on each end of the detector. Similar to the solenoid magnet, muon barrel also consists of five sections. Muon endcap is the outermost endcap of the CMS and the HF lies just outside of this endcap.

4. HADRON CALORIMETER

The Hadron Calorimeter (HCAL) is the subdetector that detects and measures the directions and the energies of the hadrons, which are particles composed from quarks and antiquarks; such as protons, neutrons, pions, kaons etc. HCAL is an important subdetector for identifying and measuring the jets produced during the hadronization process of the quarks and gluons produced in the collisions. HCAL consists of the following subsystems: Hadron Barrel (HB), Hadron Outer (HO), Hadron Endcap (HE) and Hadron Forward (HF) (Figure 4.1) [5]. These subdetectors will be briefly discussed below except the HF detector. The HF detector will be described in detail in the next chapter.

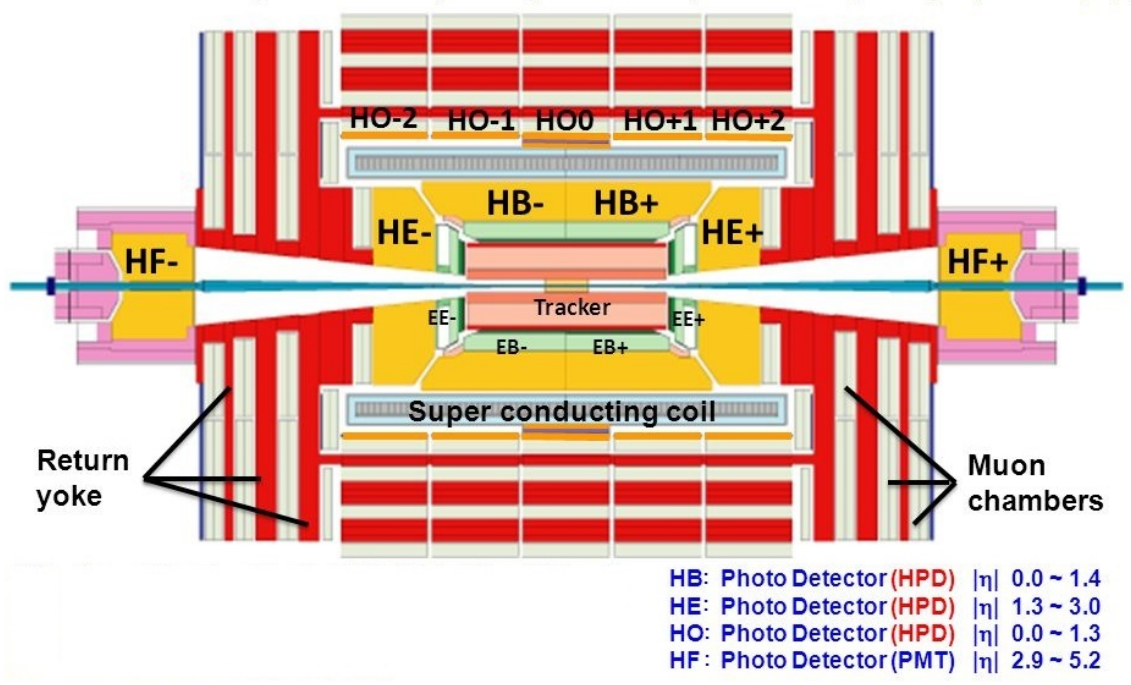

Figure 4.1. Positions of the subsystems of the HCAL subdetector. The +z direction is towards the right [6].

4.1. Hadron Barrel

Hadron Barrel (HB) is a cylindrical subdetector that lies just outside the ECAL and just inside the magnet. It has two half-cylinders, one on −z side and the other one on +z side. Each cylinder consists of 18 absorber wedges and each wedge is made from a brass alloy (90% Cu, 10% Zn), except for the innermost and outermost layers, which are made from stainless steel for the purpose of the mechanical strength of the structure. HB detects particles within the pseudorapidity range of $|\eta| < 1.4$. For the scintillation of the showers, plastic scintillator tiles are used. The scintillation light is then collected by wavelength shifting (WLS) fibers. Then this light is read out by hybrid photodiodes (HPD).

4.2. Hadron Outer

HB is a hollow cylinder that lies between the radii $r = 1.806m$ and $r = 2.950m$, which makes it less than a meter deep, due to several constraints. To compensate with this low interaction depth, there is another layer of scintillating tiles and WLS fibers between the magnet and the first layer of the muon system, which is called the Hadron Outer (HO). Just like the solenoid magnet and the muon system, it consists of five sections, as seen in Figure 4.1. The light output from the fibers are read by HPDs connected to a separate channel. It is a subsystem of the HCAL that covers the pseudorapidity range, $|\eta| < 1.3$.

4.3. Hadron Endcap

Hadron Endcap is the name for the two caps that lie at the ends of the HB. It is made from the same brass alloy that is used in the HB. Scintillation material is also the same as in the HB. It also has 18 wedges and covers the pseudorapidity range $1.3 < |\eta| < 3$.

5. HADRON FORWARD CALORIMETER

The Hadron Forward (HF) Calorimeter is in the forward region of the CMS ($3 < |\eta| < 5$) and is very important in detecting and identifying the events that produce forward jets. It also improves the determination of the missing transverse energy.

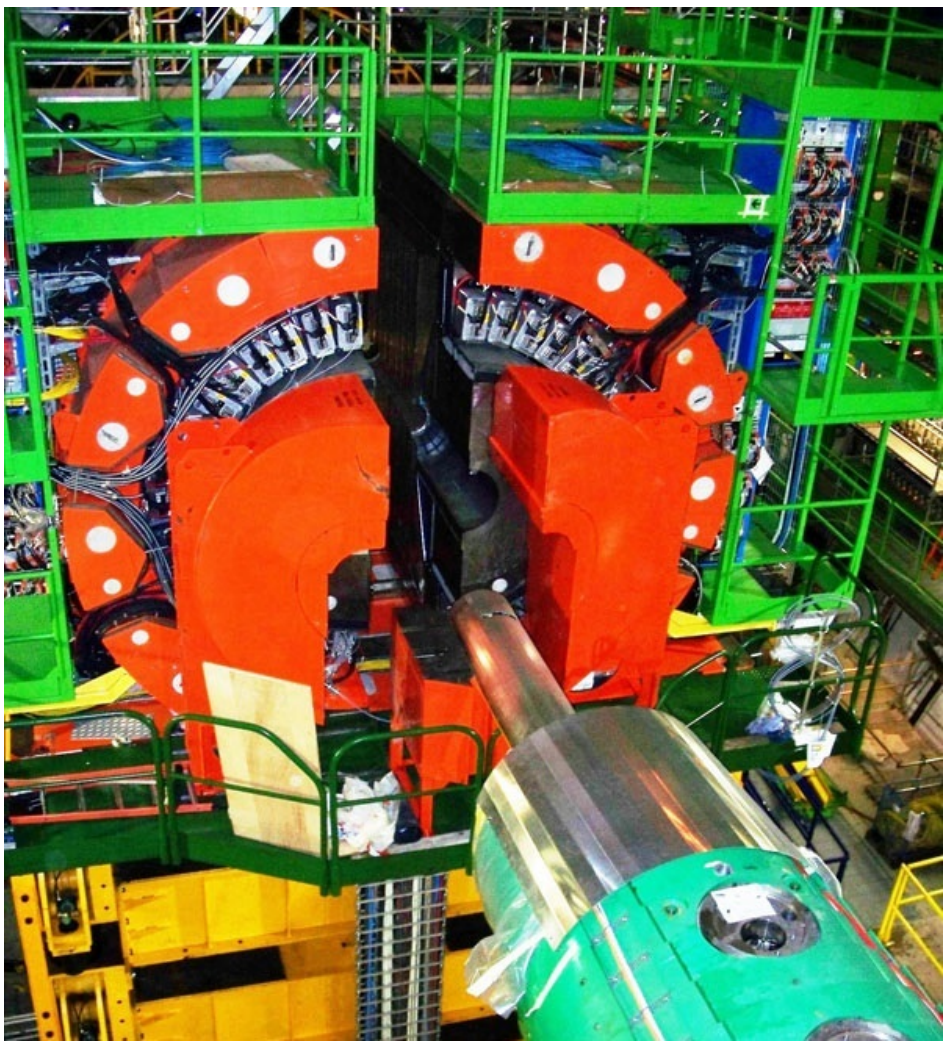

Figure 5.1. One of the HF detectors seen from the beam pipe towards the IP [7].

There are two components of the HF, which are called HF+ and HF−, on either side of the CMS, both being just outside the muon endcaps (Figure 5.1). They are 11

m away from the Interaction Point (IP). The sensitive part of each HF detector is a steel cylinder with an outer radius of 130 cm and an inner radius of 12.5 cm. The beam pipe passes through the central hollow part of both of these cylinders and is made of beryllium. Lengths of these cylinders are 165 cm and they are oriented so that they are coaxial with the beam pipe. Each of these cylinders consists of 18 identical wedges (Figure 5.2). These wedges are essentially steel absorbers that produce the showers by absorbing the particles that result from the interactions at the IP. They are also fitted with quartz fibers to produce Cherenkov light from these particle showers. Cherenkov Radiation is an electromagnetic radiation emitted by charged particles moving faster than the speed of light in a medium. Slower particles do not emit Cherenkov radiation, therefore HF is "blind" to the slower particles. The radiation pattern is a cone of light centred along the path of the charged particle. Once it is produced inside the fiber, the Cherenkov light is carried into the PMT by the same quartz fiber. Intensity of the Cherenkov light produced in the fibers is proportional to the energy of the incoming particle that produces the shower. Thus, the energy of each incident particle is measured by counting the photons with the PMTs. [8] These quartz fibers are made out of a fused silica core (600 μm diameter), a polymer hard-cladding (15 μm thickness) and a protective acrylate buffer (85 μm thickness). Each quartz fiber has an overall diameter of 800 μm. [9]

The fibers are laid out in two different lengths in each wedge. Half of them are long fibers and the other half are short fibers. Long fibers run all the way through each wedge from the surface of the side that faces the IP to the Readout Boxes (ROBOX), which are basically light tight boxes that house the PMTs. Short fibers also run to the ROBOXs, but they start at 22 cm deep from the side that faces the IP. These two different lengths of fibers serve for different purposes, thus are read separately.

Figure 5.2. One of the steel wedges of the HF with its quartz fibers attached. Mounting slots for ROBOXs can also be seen. [10]

It can clearly be seen from Figures 3.1 and 4.1 that there is no absorber material between the IP and the HF on either side of the CMS. The reason for this is that the EM part of the showers from particles emerging from the IP in the $3 < |\eta| < 5$ region can also be absorbed by the steel wedges of the HF.

Electromagnetic showers occur mostly at the beginning of the absorber in the HF detector. These showers are mostly detected by the long fibers. But unlike the EM showers, hadrons from the IP are absorbed gradually throughout the whole wedge, while most of them producing showers deeper than the EM showers. We also get some signals from the hadrons that were absorbed in the first 22 cm. So the signal from the long fibers is a mixture of the signals from EM and hadronic particles. But after 22 cm of depth, there are very few purely-EM-interacting particles left to be absorbed by the absorber, thus the short fibers only detect the hadronic particles.

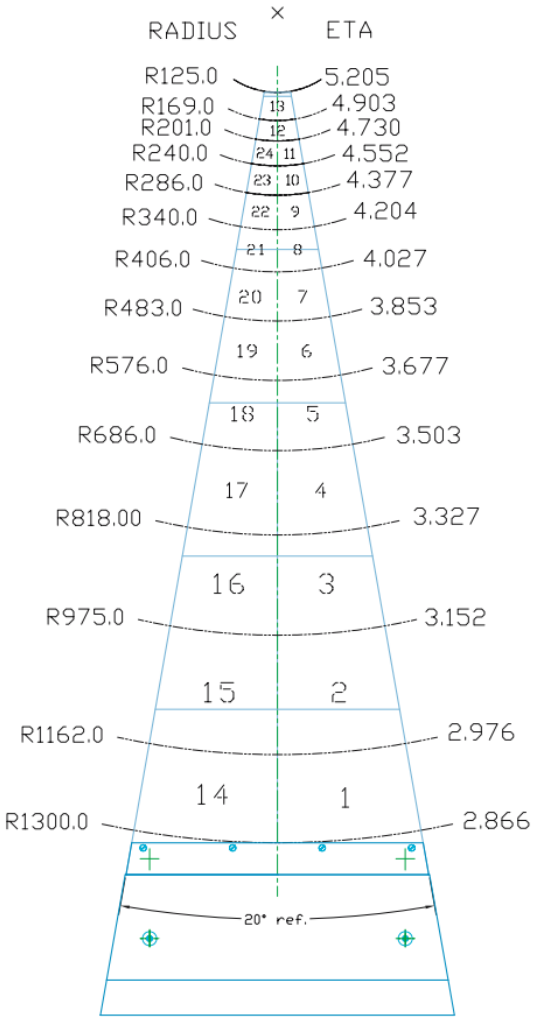

Figure 5.3. Tower configuration of an HF wedge. [8]

Each wedge is divided into 24 towers (Figure 5.3) and each tower is fitted with both long and short fibers (Figure 5.4). As mentioned before, long and short fibers are read out separately, hence signals from each tower is read out using two PMTs. Since each wedge has 24 towers, 48 PMTs per wedge are needed to be able to read the signals properly. Having 18 wedges on either side of CMS, the number of PMTs needed for the whole HF system is 1728. Apart from the quartz fibers, there is also a radioactive source wire installed on each tower for the purpose of the calibration of the detector.

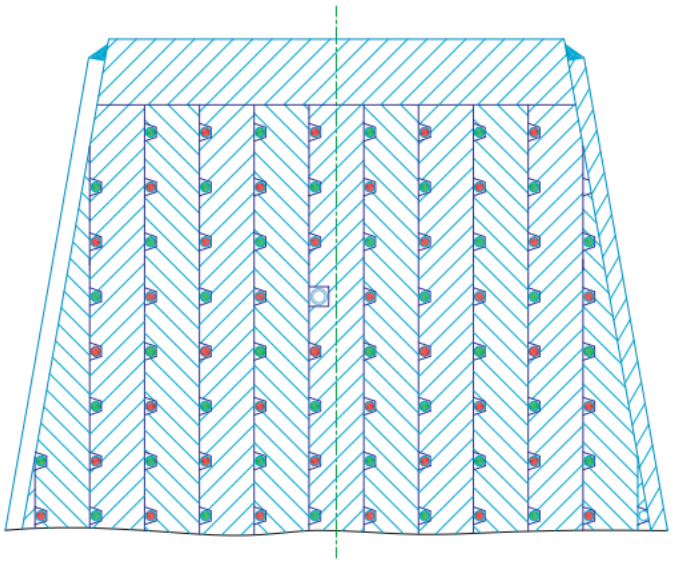

Figure 5.4. Fiber configuration of a tower (#13). (Red: Short fibers, Green: Long fibers, White: Radioactive source wire) [8]

Azimuthal size of all wedges are $\Delta\phi = 20°$. Tower heights decrease as they get closer to the beamline. This is for keeping a constant value of $\Delta\eta = 0.175$ between all vertically adjacent towers except for towers 1, 13 and 14. Except for towers 12 and 13, each tower has a $\Delta\phi = 10°$, and if we convert this angle into radians, we get $\Delta\phi = 0.175$. Thus for most of the towers, we have a relationship of $\Delta\eta \times \Delta\phi = 0.175 \times 0.175$. Full table of pseudorapidities and azimuths are given in Table 5.1 below.

Table 5.1. Table of inner and outer radii, angles, pseudorapidities, number of fibers attached and total fiber cross sections for each wedge (N_{fib}: Number of fibers attached on a wedge, A_b: Total fiber bundle cross section of a wedge). [8]

Ring	r_{in}, r_{out} **(mm)**	$\Delta\eta$	$\Delta\phi$ **(deg.)**	N_{fib}	$A_b(mm^2)$
1	1162-1300	0.111	10	594	551
2	975-1162	0.175	10	696	652
3	818-975	0.175	10	491	469
4	686-818	0.175	10	346	324
5	576-686	0.175	10	242	231
6	483-576	0.175	10	171	167
7	406-483	0.175	10	120	120
8	340-406	0.175	10	85	88
9	286-340	0.175	10	59	63
10	240-286	0.175	10	41	46
11	201-240	0.175	10	30	35
12	169-201	0.175	20	42	52
13	125-169	0.300	20	45	50
14	1162-1300	0.111	10	594	551
15	975-1162	0.175	10	696	652
16	818-975	0.175	10	491	469
17	686-818	0.175	10	346	324
18	576-686	0.175	10	242	231
19	483-576	0.175	10	171	167
20	406-483	0.175	10	120	120
21	340-406	0.175	10	85	88
22	286-340	0.175	10	59	63
23	240-286	0.175	10	41	46
24	201-240	0.175	10	30	35

5.1. Photomultiplier Tubes

PMT system is used for reading out the photons that arrive from each set of fibers coming from each tower of HF. Long fibers and short fibers are read out separately, which means that there are 2 PMTs that read out each tower, as mentioned before. PMTs are grouped in readout boxes (ROBOX). Each ROBOX contains 24 PMTs arranged in a 6 by 4 array, connected to a single baseboard. Since each wedge has 24 towers, two ROBOXs per wedge are needed to readout 24 pairs of fiber bundles that emerge from each tower. When HF was built, Hamamatsu R7525 single anode PMTs were used (Figure 5.5). It has 8 dynode stages and a bialkali photocathode with a diameter of 25 mm. Its front window is made from borosilicate glass and is 1 mm thick at the centre and 6.1 mm thick at the edges. Quantum efficiency of this PMT is 23% for 450 nm of wavelength. This PMT has an anode pulse rise time of 1.3 ns and an electron transit time of 14 ns. These times are adequate for the purpose of the HF, since each bunch crossing at the LHC takes 25 ns. [11]

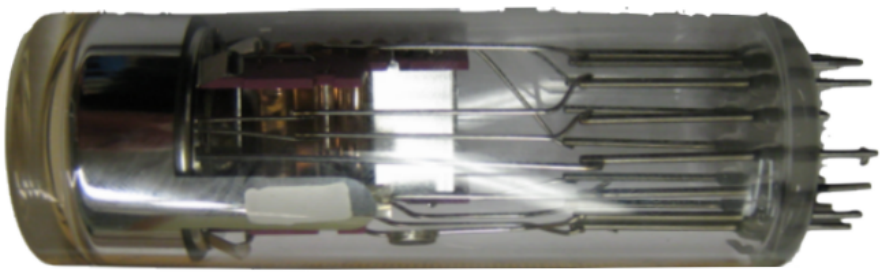

Figure 5.5. Hamamatsu R7525 single anode PMT [12].

5.2. PMT Upgrade

As the energy and the luminosity of the LHC was being increased gradually, some major problems started to occur. One of them was the PMT afterpulse issue. Afterpulses are small signals with a few photoelectron level that occur after the main

pulse. There are two types of afterpulses (Figure 5.6). First one is the short delay afterpulse, which occurs tens of nanoseconds after the main pulse. They are caused by the elastic scattering of electrons from the first dynode. The second type is the long delay afterpulse, which occurs starting from tens of nanoseconds up to several microseconds after the main pulse. This type of afterpulse occurs mostly due to the ionization of residual gas molecules inside the PMT. In HF's case, the problem was the long delay afterpulse. This is thought to be caused by the degradation of the vacuum of the PMTs due to the seepage of helium gas which is present in the HF's environment. Even though this was a rare occurance (3-4%) for the old PMTs, it was still sufficient to spoil the data. The proposed solution to this problem was to displace the helium in the ROBOXs by constantly pumping nitrogen gas into them.

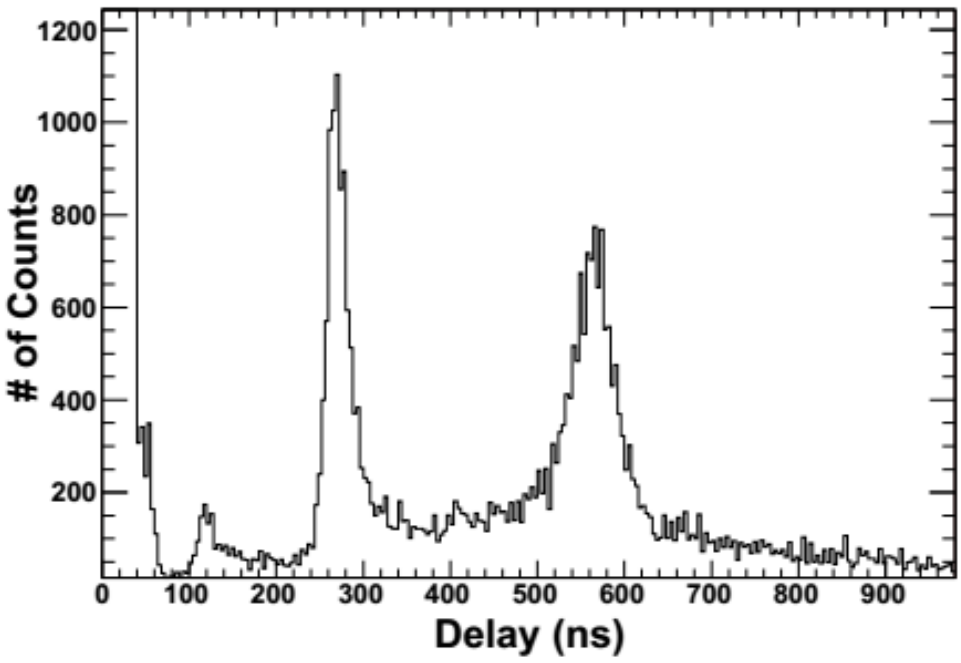

Figure 5.6. Afterpulse delays of one of the Hamamatsu R7525 PMTs from the HF with respect to the main signal. [13]

The other issue about the old PMTs is the so called window events. The PMTs are normally isolated from the incoming radiation from the IP by radiation absorbing

tiles placed between the wedges and the ROBOXs. Most of the incoming high energy particles (EM and Hadronic) that are inbound to the PMTs are absorbed by these tiles with the exception of muons, since they have a very low absorption rate through the interaction with ordinary matter. But when they hit the front window of one of the PMTs, they cause Cherenkov radiation while passing through the front window. This was a known issue since the very beginning of the HF and it was not considered as a huge problem at the time, because the "real data" coming from the quartz fibers and the anomalous signals coming from the window events were easily distinguished by comparing the signals from the long and short fibers. Real events have simultaneous signatures on both PMTs, since both EM and hadronic showers leave signatures on both fibers, whereas window events usually leave a signature on a single PMT. But as the beam luminosity of the LHC increased, simultaneous window events started to occur on both PMTs related to the same wedge and get mistakenly recorded as real events. First step to resolve this issue was to reduce the window event rate itself via changing the PMTs. This was done in the Long Shutdown 1 period of the LHC. All Hamamatsu R7525 PMTs in the HF were replaced with Hamamatsu R7600U-200-M4 PMTs (Figure 5.7). This is a 4-anode PMT with a quantum efficiency of 40% at around 400 nm, which is significantly larger than the former PMTs. Window material for this PMT is again borosilicate glass, however its thickness is less than 1 mm, which makes it significantly thinner than the older PMTs.

The performance of the new PMTs are significantly better than the old ones. Due to the thinner windows, window event rate has reduced significantly. Similarly, the real data response is also improved due to higher quantum efficiency (Figure 5.8). Also, having PMTs with multiple anodes allowed the possibility to read each fiber bunch using multiple channels and therefore distinguish the real signals from the window events even better, since a real event would leave a signature on all anodes, wheras a window event would leave a signature usually on a single anode.

Figure 5.7. Hamamatsu R7600U-200-M4 4-anode PMT.

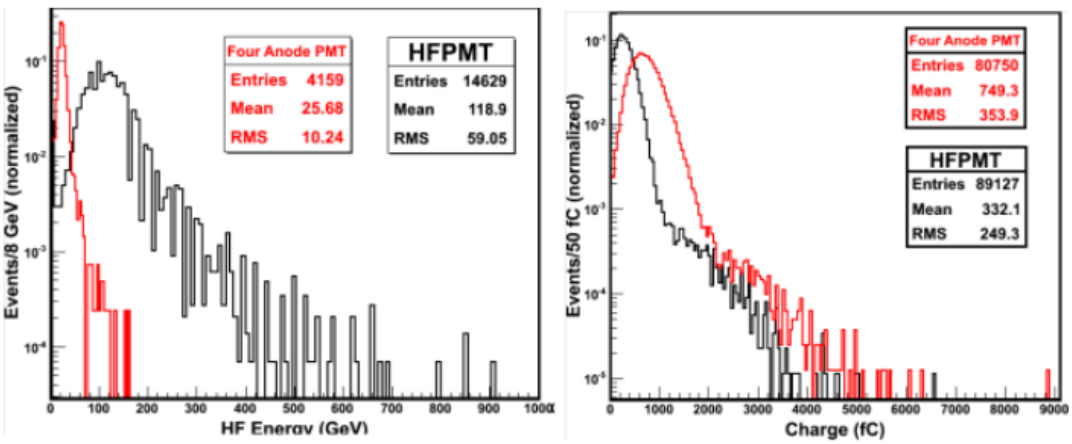

Figure 5.8. Left: Comparison of window event data between single anode PMTs and 4 anode PMTs. Number of window events are significantly reduced due to the thinner window of the new PMTs. Right: Comparison of real data between single anode PMTs and 4 anode PMTs. Sensitivity is increased due to the higher quantum efficiency of the new PMTs. [14] [15]

6. HF-FE ELECTRONIC CARDS

6.1. DAQ System

The data acquisition (DAQ) system consists of two main parts: frontend (FE) and backend (BE). Frontend is the hardware that acquires the signal from the PMTs, converts it to digital data and sends it to the backend. This work is done by the QIE cards. On the BE, the digital data from the QIE cards are sent to μHTRs. They are the hardware that get the digital data and calculate the trigger primitives. FE and BE are on different types of crates. But the frontend is sychronized with the backend via a card called new generation clock control module (ngCCM) that is housed in the FE, which is connected to the backend with a fiber optic cable.

6.2. QIE Cards

QIE cards are the electronic hardware that acquires the analog signals from the PMTs and convert them into digital data. They are the main scope of this upgrade. These cards have 24 analog input channels, thus each card can process 24 different signals simultaneously. Due to the new configuration, each PMT will be read by two channels, which means that each QIE card will read signals from 12 PMTs. These PMTs are going to be connected into the Winchester connectors in front of the cards. A total of 144 cards will be needed in the HF for this new readout scheme.

Each one of these 24 channels is fed into one of the 24 QIE chips, located on a given QIE card. There, all 24 signals from the inputs are integrated separately within 25 ns intervals, then the results are converted into digital data. This digital data is then sent to two Igloo2 FPGAs. Here, the data from the QIE chips are reformatted, serialized and sent to the VTTxs as six serial data lines. VTTxs are devices that convert the electrical data signals into optical signals. Each VTTx can convert two electrical data signals into two optical data signals. These optical signals are then fed to the BE system. There, the data are deserialized, important events are selected by

the trigger and sent to the GRID to be processed.

QIE cards are mounted in a crate and connected to the backplane of that crate. Each crate is powered by an 8V DC power supply through the backplane. This power is then fed to five DC-DC converters and converted to 1.5V, 2.5V, 1.2V, 3.3V and 5V on the QIE cards. Most of the chips on the cards run at 3.3V. However, to be able to run the FPGAs, various different voltage levels are needed. The main components of the QIE cards are discussed below. Different parts of the QIE cards are shown in the Figures 6.1 and 6.2.

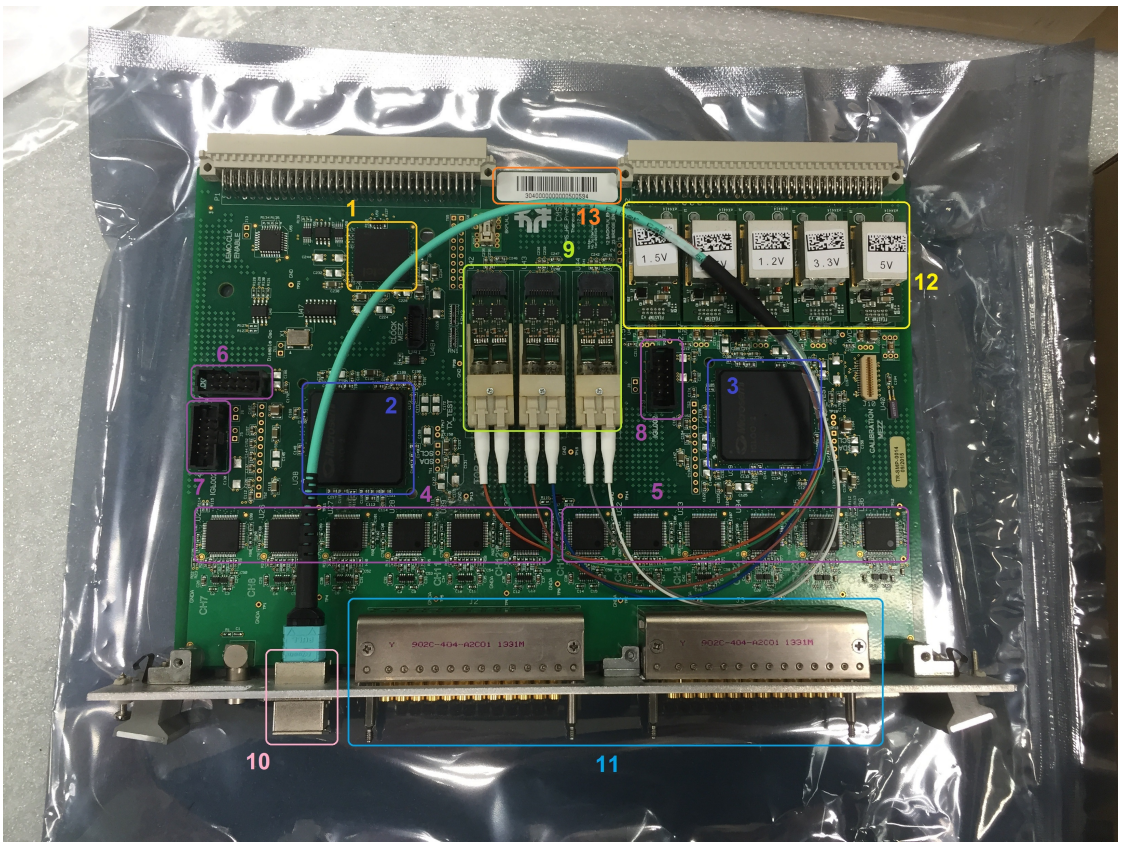

Figure 6.1. Front face of a QIE card with its components numbered as; 1: Bridge FPGA, 2: Top Igloo2 FPGA, 3: Bottom Igloo2 FPGA, 4: Top QIE10 Chips (Channels 7-12), 5: Bottom QIE10 Chips (Chan. 19-24), 6: Bridge FPGA programming port, 7: Top Igloo2 programming port, 8: Bottom Igloo2 programming port, 9: VTTx, 10: MTP connector, 11: Winchester connectors (PMT inputs), 12: DC-DC converters. 13: CMS identification sticker

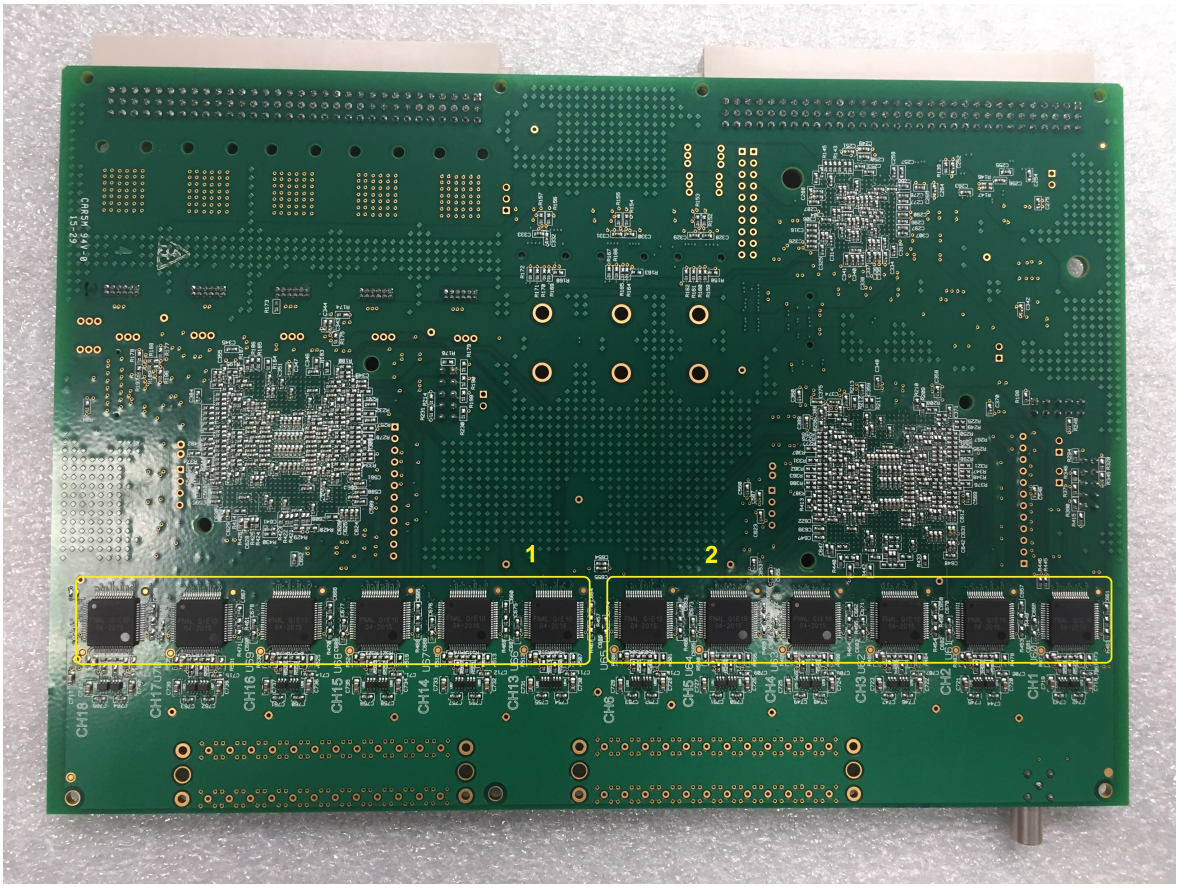

Figure 6.2. Back face of a QIE card. The remaining 12 QIE chips are on this side (1: Bottom QIE10 chips (Chan. 13-18), 2: Top QIE10 Chips (Chan. 1-6)

6.3. QIE10 Chips

These chips are basically the ADCs that take the PMT signal and convert it to digital data for the new QIE cards. Their analog inputs are connected to the Winchester connectors in front of the card and their digital outputs are connected to the Igloo2 FPGAs. These chips are divided into two groups on each card, which are called the top QIE chips and the bottom QIE chips, as shown in the Figures 6.1 and 6.2. There are 12 top QIE10s (6 on either face) and 12 bottom QIE10s (6 on either face) on each QIE card. These chips are designed to acquire and accurately measure the PMT signals. This means that these chips need to deal with negative voltages on their analog inputs. A QIE10 chip first acquires the signal as a current pulse from

the PMT, then it integrates that incoming signal within 25 ns intervals in order to get the amount of charge injected into the analog input on each 25 ns period, converts this into an ADC value and sends it out via a data line. Reason for the integration interval being 25 ns is that the bunch crossings at the LHC lasts for 25 ns. These 25 ns intervals are also divided into 16 clock phases (each being 1.5625 ns long), in order to match the timing of the integration intervals with the PMT signals. The integration is done by storing the charge injected by the PMTs in on-chip capacitors. One capacitor is used for each 25 ns cycle and there are four of these capacitors in each QIE10 chip. That is because it takes time to read the value and to empty a capacitor in order to prepare it to its next cycle. Capacitors are also labeled with numbers from 0 to 3, which are called Cap IDs. Cap ID value is stored in a 2-bit register and sent out with the data. The digital output scale of these chips is a pseudo-logarithmic scale, not a linear one. Charge difference between two adjacent bins change with the amount of charge injected to the input channel of the QIE10 chip in one period. This is done in order to make the relative input charge resolution not to vary too much. This scaling is done by dividing the input charge range into four ranges and dividing each range into four subranges. The bin "sensitivities" for different charge and ADC value ranges are shown in Table 6.1. On this table we can see that within each range, the ADC value (so called "Mantissa") can be between 0 and 63, wheras range information can take a value from 0 to 3. By this, we can see that the mantissa is a 6-bit value, and the range is a 2-bit value. So, the ADC is an 8-bit value in total. Also, there are intentionally constructed range overlaps in order to prevent gaps between ranges. These overlaps should be removed via calibration in order to prevent range collisions.

The QIE chips also have a TDC functionality. TDC is basically a timer that measures the arrival time of the first rising edge of an input pulse. It divides each 25 ns period into fifty 500 ps intervals. Since TDC can take values between 0 and 49, it can be represented as a 6-bit value. If we add up the number of bits of ADC, TDC and Cap ID, we get a total of 16 bits per 25ns, which makes the frequency of this data line 40 MHz. There is also a synchronizer inside each QIE10 chip that converts this 16-bit 40 MHz data line into an 8-bit 80 MHz one.

Table 6.1. ADC value versus input charge-sensitivity table for QIE10 chips. [16]

Range (Exp.)	**Input Charge**	**ADC (Mant.)**	**Sensitivity (Q/bin)**
0	−16 fC - 34 fC	0 - 15	3.1 fC/bin
0	34 fC - 158 fC	16 - 35	6.2 fC/bin
0	158 fC - 419 fC	36 - 56	12.4 fC/bin
0	419 fC - 592 fC	57 - 63	24.8 fC/bin
1	517 fC - 915 fC	0 - 15	24.8 fC/bin
1	915 fC - 1910 fC	16 - 35	49.6 fC/bin
1	1910 fC - 3990 fC	36 - 56	99.2 fC/bin
1	3990 fC - 5380 fC	57 - 63	198.4 fC/bin
2	4780 fC - 7960 fC	0 - 15	198.4 fC/bin
2	7960 fC - 15.9 pC	16 - 35	396.8 fC/bin
2	15.9 pC - 32.6 pC	36 - 56	793.6 fC/bin
2	32.6 pC - 43.7 pC	57 - 63	1587 fC/bin
3	38.9 pC - 64.3 pC	0 - 15	1587 fC/bin
3	64.3 pC - 128 pC	16 - 35	3174 fC/bin
3	128 pC - 261 pC	36 - 56	6349 fC/bin
3	261 pC - 350 pC	57 - 63	12.70 pC/bin

6.4. Igloo2 FPGA

Each of these FPGAs get 12 QIE10 chips worth of data, serialize them into three 5Gbps serial data lines and sends the output into the VTTxs.

6.5. VTTx

Versatile Twin Transmitters (VTTx), shown in Figure 6.1, convert the digital serial data lines into optical data. One VTTx can convert two serial data lines simultaneously. Since there are two Igloo2 FPGAs on each card, three VTTxs are needed in order to be able to send the data. These devices are custom-made by CERN.

6.6. Bridge FPGA

Bridge FPGA provides the communication of the FE backplane with all the QIE10 chips, Igloos and various other interfaces on the QIE card. Model of the FPGA used for this purpose is Actel ProASIC 3.

6.7. Production of the QIE cards

The electronics design and the component layout of these cards were done at Fermilab, PCBs were manufactured in the USA and the components were mounted on the PCBs at a company named SimPro, which is located in Istanbul, Turkey [17]. Nearly all components on this board are surface mount devices (SMD), so most of the soldering job is done by reflow process. In this process, solder paste, which is basically a suspension mixture of solder flux and little solder balls, is applied on the electrical contacts on the board that will be joined to the contacts of the components. Then the components are placed on the board. Since this is a mass production and each card has hundreds of components on it, a pick and place machine is used for the component placement of the boards. Afterwards, the boards are driven into a temperature controlled oven with a conveyor belt inside, called a reflow oven. Inside, the solder melts and the components are joined together with the board.

First, solder paste was applied on the front face of the board. Then, that face was populated with components and afterwards, the board was put into the reflow oven. After the reflow of this face, solder joints were checked for defects. On the front face, contacts on all the components except for both Igloo2 FPGAs and the Bridge FPGA

are on the sides of their packages. These three chips however, have their contacts directly under their packages. This type of package is called a ball grid array (BGA). The inspection was first done visually, in order to check the solder job on the board and the directions of the components. Then, x-ray imaging is used for the inspection of BGA components, since it is impossible to conduct reliable visual inspection on solder joints that are under the chips. One of the x-ray images are shown in Figure 6.3.

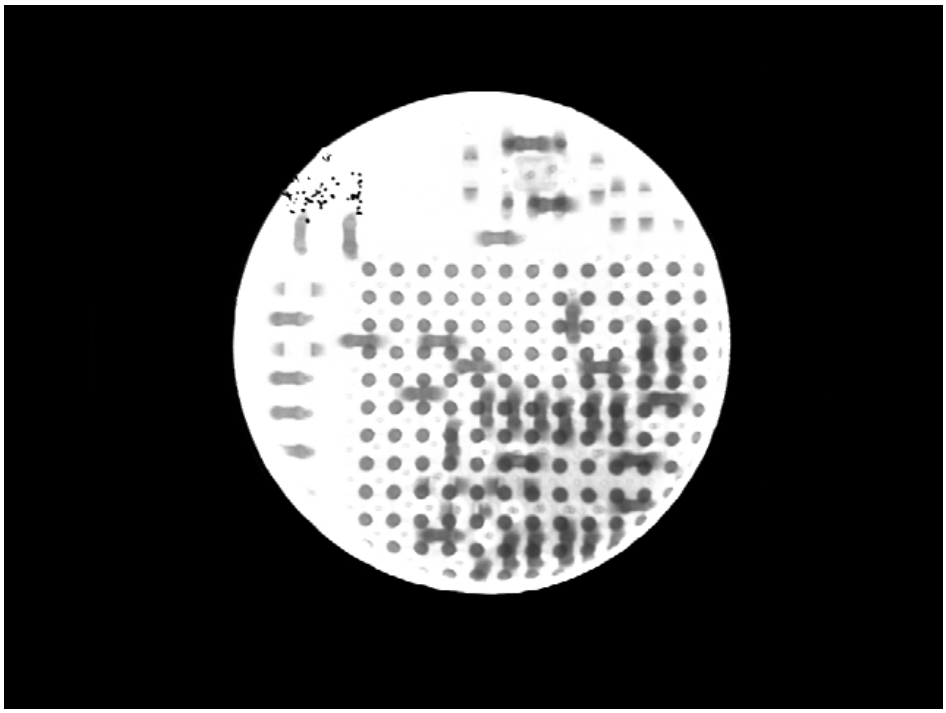

Figure 6.3. Top left x-ray image of a bridge FPGA. Solder balls and some components on the other face of the board are visible.

After the inspection, defective solder joints (e.g. cold solder joints, trapped air bubbles) were fixed. Afterwards, the back side of the board was pasted, populated with components, reflowed and inspected using the same procedure. Later, all the solder joints were checked by x-ray imaging again. There were also some through hole components that should be soldered on the boards, such as Winchester connectors, 10-pin programming ports for the FPGAs, VME connectors that connect the QIE cards to the FE backplane etc. They were soldered by hand after the reflow of both sides of the card (Figure 6.4). Then the boards were washed in order to clean the solder flux

residues from them. Finally, they were put in an antistatic packaging (Figure 6.5) and shipped to CERN.

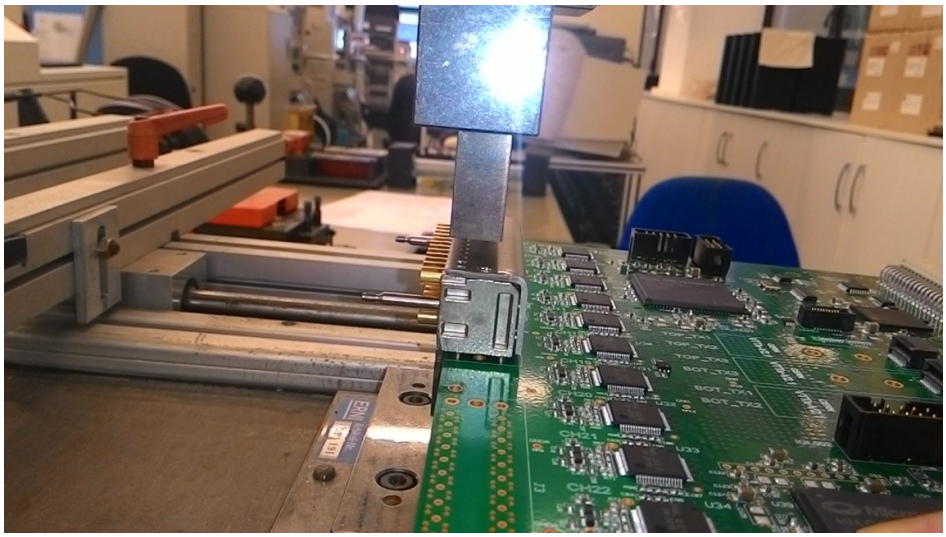

Figure 6.4. A Winchester connector getting ready to be hand-soldered on the QIE board.

Figure 6.5. Cards are being packed for shipping.

7. TESTING THE HF-FE CARDS

We had 200 QIE cards delivered to CERN on September 2015. 180 of them were manufactured completely, however the QIE10 chips were not mounted on the remaining 20 cards. Also, most of the Winchester connectors had not yet been installed either because they were planned to be installed after testing all the cards. 144 of those 180 manufactured cards was meant to be selected for service at the UXC. The remaining ones will serve either as spare cards or as spare parts for cards.

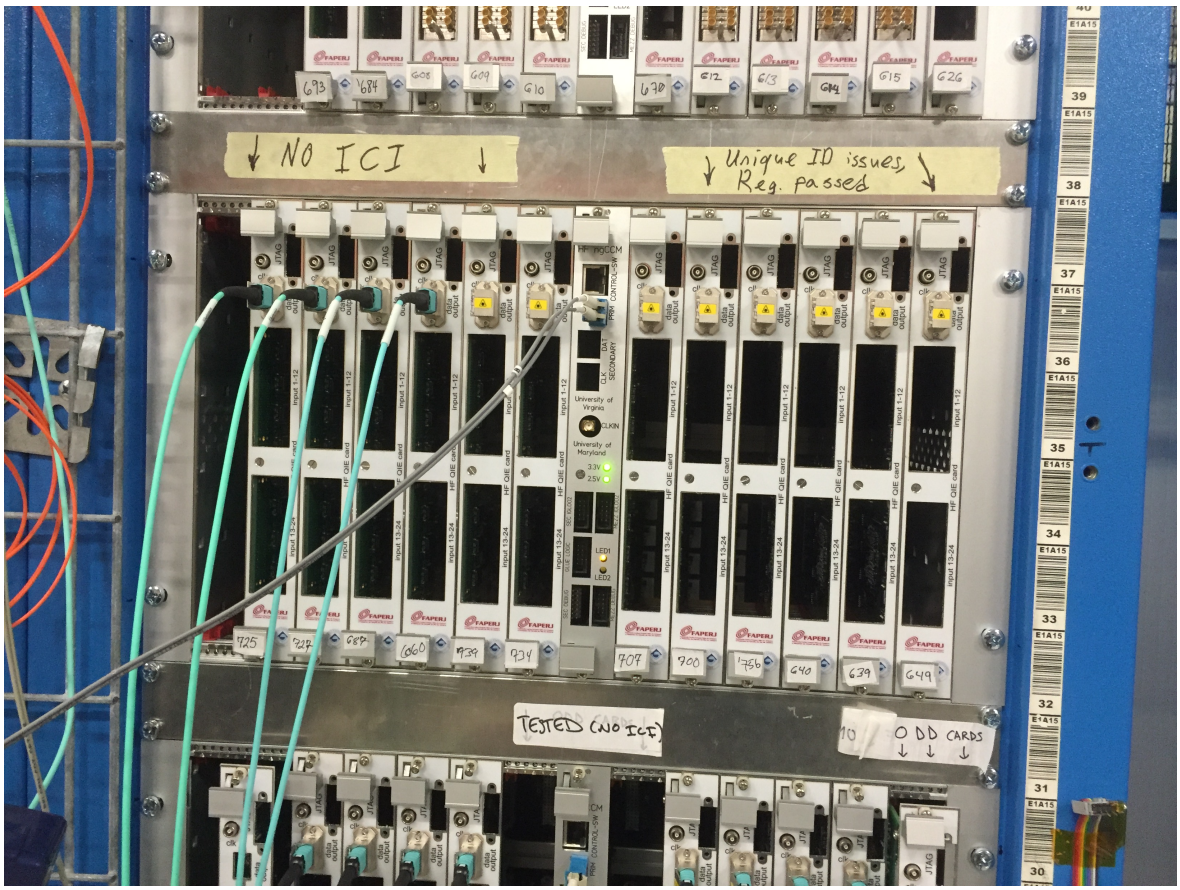

Figure 7.1. A crate filled with 12 QIE cards. There's an ngCCM in the middle.

Various tests are done to these 180 QIE cards to examine their condition and characterize their behaviour. In order to be able to test them, crates with functional backplanes were needed. First, we assembled 16 crates using their assembly kits. Then

we mounted the FE backplanes to them. Afterwards, we mounted all of the crates to the racks. Later we connected the 8V power rail to each crate (Figure 7.1).

After assembling the crates, we started to assemble, examine and test the cards. First we did a visual inspection in order to assess the cards if they have visual defects (e.g., missing components, cracks, scratches) on them. All of the cards were visually satisfactory (Figure 7.2).

Figure 7.2. QIE card without VTTxs, DC-DC converters and front plates.

After the visual inspection, we stuck the CMS identification stickers, which can be seen on Figure 6.1, on these cards. Then we checked if there are any shorts between any two power rails (including the 8V backplane power rail) and between any power rail and the ground plane. We did this test with a multimeter. Next, we mounted the front plates, DC-DC converters and the VTTxs on all cards that passed the initial inspection. Afterwards, we plugged the cards into the crates and installed the firmwares

for the bridge FPGA and the Igloo2 FPGAs. Then we tested all of the cards regarding their functionality. These tests are as follows:

- Link Pattern Test: Bad data rates for the optical links between the QIE cards and μHTRs are measured. Then the Igloos are put to a test mode, so that they send a test pattern instead of the incoming digital data from the QIE10 chips. Later this test pattern is checked for corruptions (Figure 7.3).

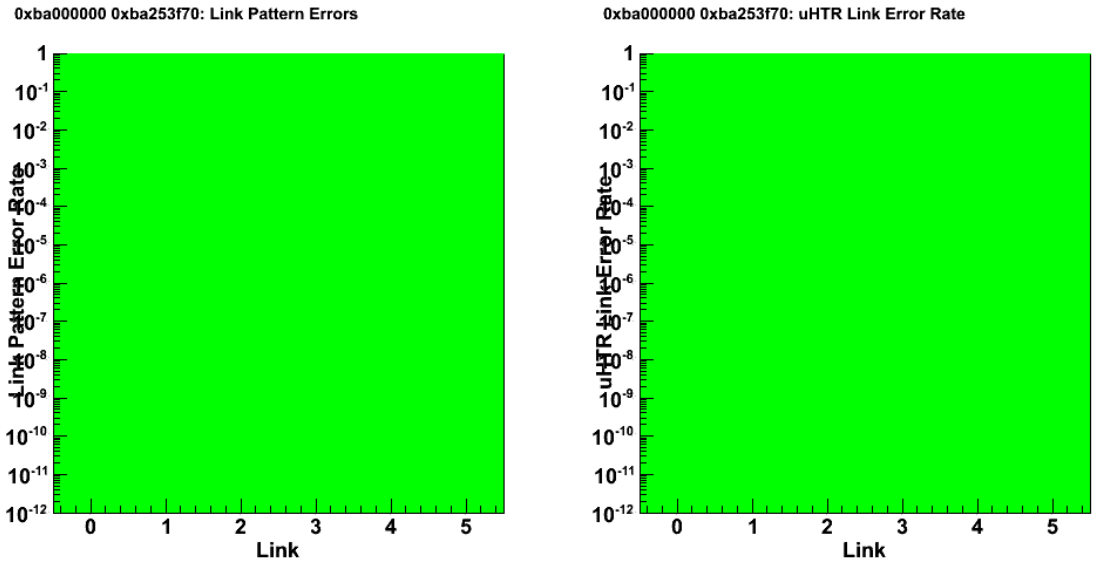

Figure 7.3. Result of a successful link pattern test.

- Register test: There are many registers on the bridge FPGA, igloo FPGAs and QIE10 chips of each QIE card. These registers are used for the storage of the data, setting and mode information for a QIE card. In this test, each register is written with random data. Then this random data is read, and then written and read values are compared in order to examine the registers for read/write errors. Five read/write cycles are done per register (Figure 7.4).

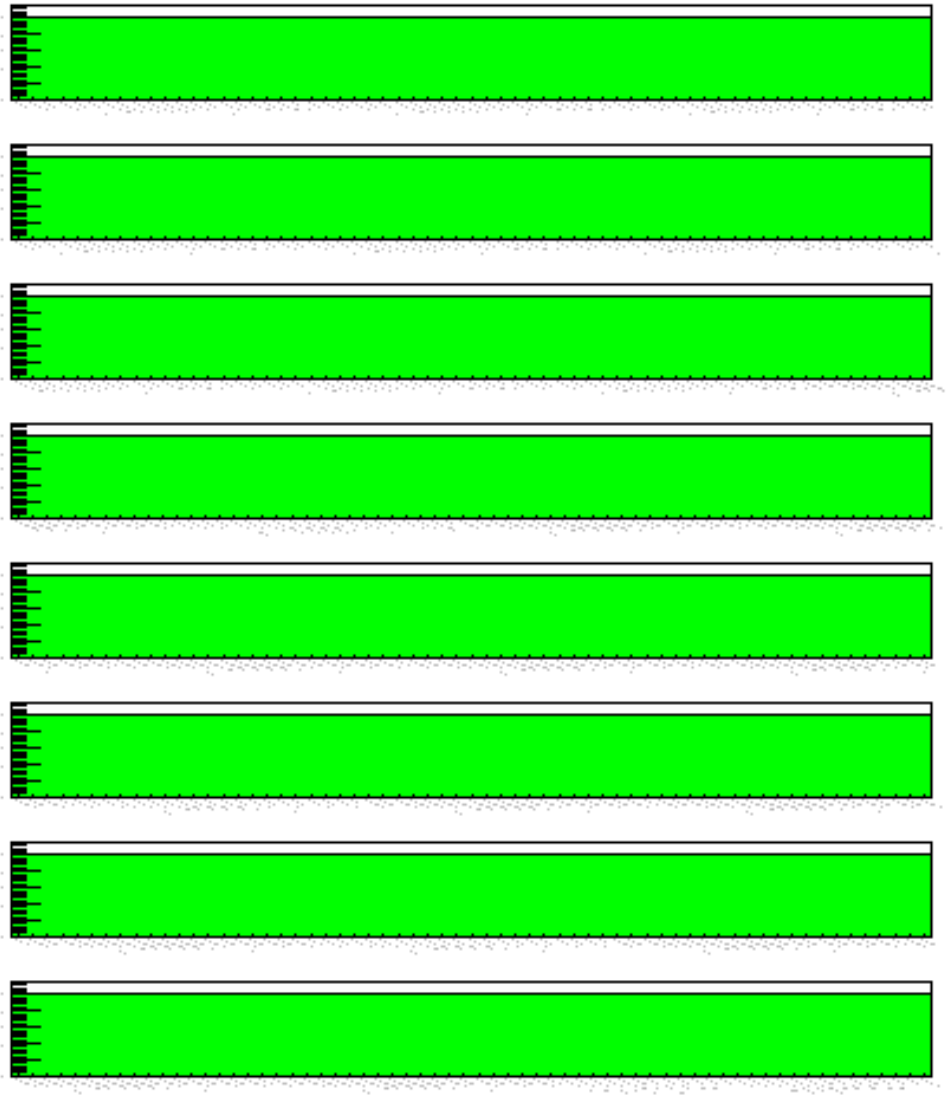

Figure 7.4. Result of a successful register test. The first seven rows and left half of the bottom row show the status of the registers involving QIE chips. Right half of the bottom row represents the Igloo2 registers.

- Pedestal test: Pedestal values of all chips on every card are read and the ADC values are put to a histogram. Pedestal histogram for a good QIE10 chip should have a mean ADC value around 4 and a standard deviation around 2 (Figure 7.5).

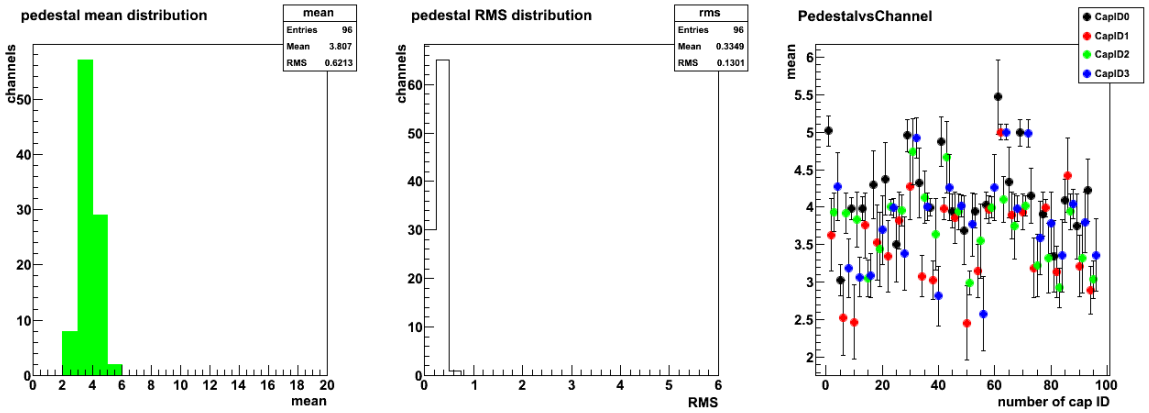

Figure 7.5. Result of a successful pedestal test. Histogram to the left shows the pedestal ADC value distribution of all QIE10 chips over all Cap IDs on a QIE card. This value should be between 2 and 6. Histogram to the right shows the raw data of this distribution.

- Cap ID test: Each capacitor that stores the analog signal has an ID from 0 to 3. All QIE chips are tested if these cap IDs rotate in the correct order within all 16 clock phases (Figure 7.6).

It is possible to communicate with the QIE cards by using various executable tools that connect to the DAQ system from a PC. All of these tools have a command line interface. We only needed two of these tools to create our test scripts. One of these tools is called ngFEC. It is a tool used for reading and writing the registers of the QIE cards. It communicates with the cards via the ngCCM and through the FE backplane. The other tool is called the uHTRtool. It is a tool that fetches the raw data from the μHTR that is sent from the QIE cards. The test scripts were written in python. They run the executable tools, send the necessary commands, read the printout and record the results into a histogram.

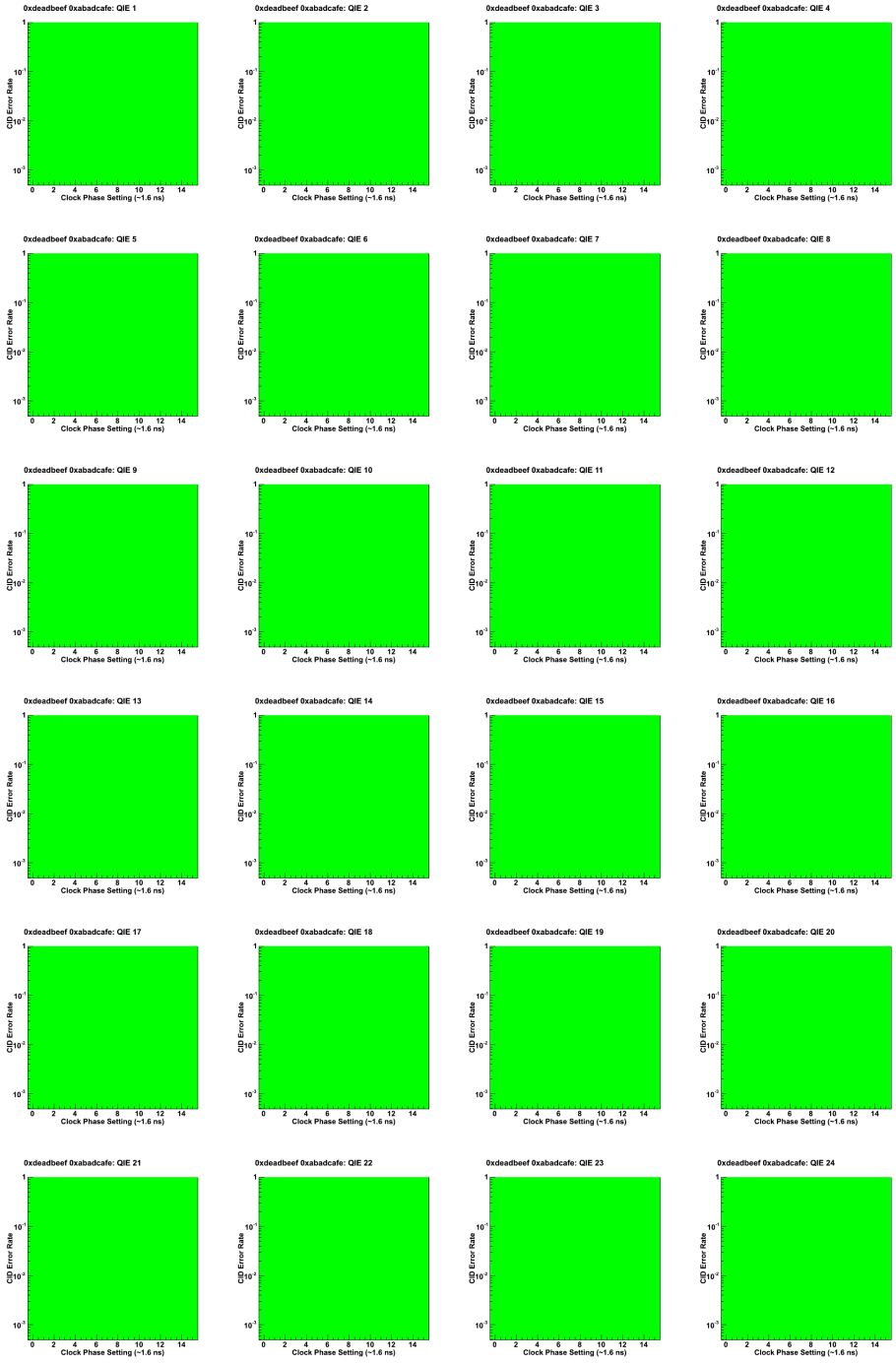

Figure 7.6. Result of a successful Cap ID test. Each histogram corresponds to one QIE chip. The horizontal axis of each histogram represents the clock phase setting. Each row of histograms represents an Igloo2 link.

7.1. Results of the tests

While we were looking for shorts on the power and ground rails of the QIE cards, we identified 4 cards with shorts on their power rails. These cards were later sent to Fermilab for further inspection. When we first did the tests, we encountered bad link problems on 2nd and 5th VTTx links. Because of this, we were seeing link errors on the link pattern test, zero pedestals on the pedestal test and no cap ID information at all on the cap ID test on these two links. This issue effected nearly half of the cards. Later on, it was understood to be a timing issue on the Igloo FPGAs. This problem was solved by developing a new firmware. Only two cards suffer from this issue as of January 2016 (Figure 7.7, 7.8, 7.9).

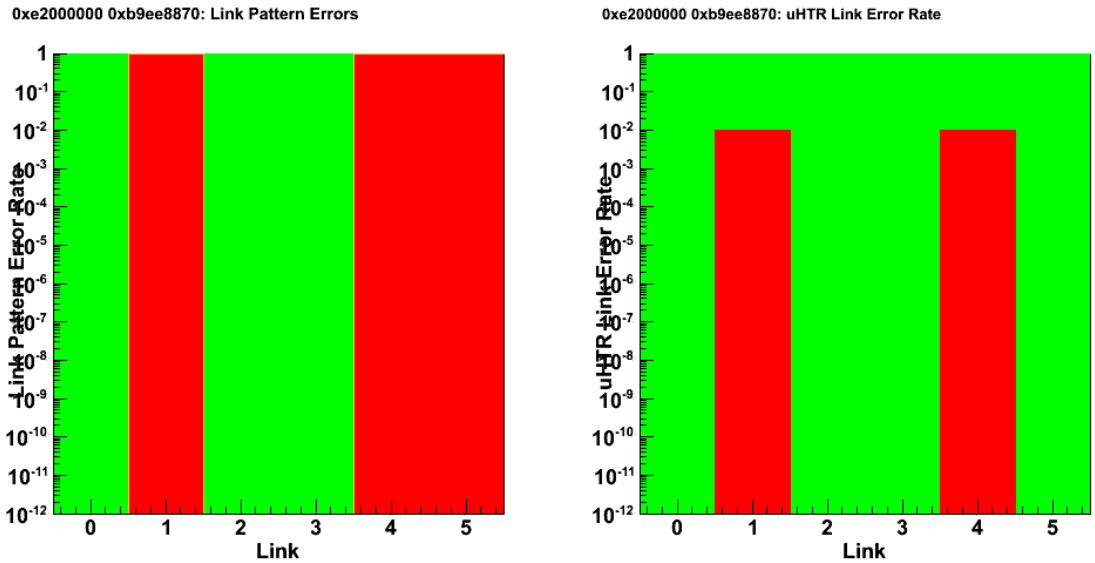

Figure 7.7. Result of a link pattern test with a middle link issue. On the right histogram, there's an error accumulation on link #4 (5th link) and link #1 (2nd link).

Another issue that we encountered was a glitch on the QIE10 chips. When the ADC value of a QIE10 chip coincides to a range transition, that chip stops functioning properly, so the card needs to be reset. Design of the chip was reviewed, the problem was found and fixed. Afterwards, some samples of this new version of QIE10 was manufactured and one QIE card was modified to have its top side QIE10s replaced with

the new ones for testing purposes. Results of the tests done to this card showed that new QIE10 chips didn't have this range transition glitch. We also had a communication issue between ngCCMs and QIE cards. For the communication between a QIE card and an ngCCM to be established, the data line between them should be high. However when we tried to read from or write to a register on a QIE card that suffers from this condition, the data line between the ngCCM and the QIE card was pulled low, thus the communication failed. We also discovered that reading from top Igloo registers or Unique ID register particularly triggers this problem. Afterwards we found out that the issue was most likely to be caused by the Bridge FPGA. The results of the attempts to fix the firmware for the Bridge FPGA succeeded later on. No cards suffer from this issue as of March 2016 (Figure 7.10).

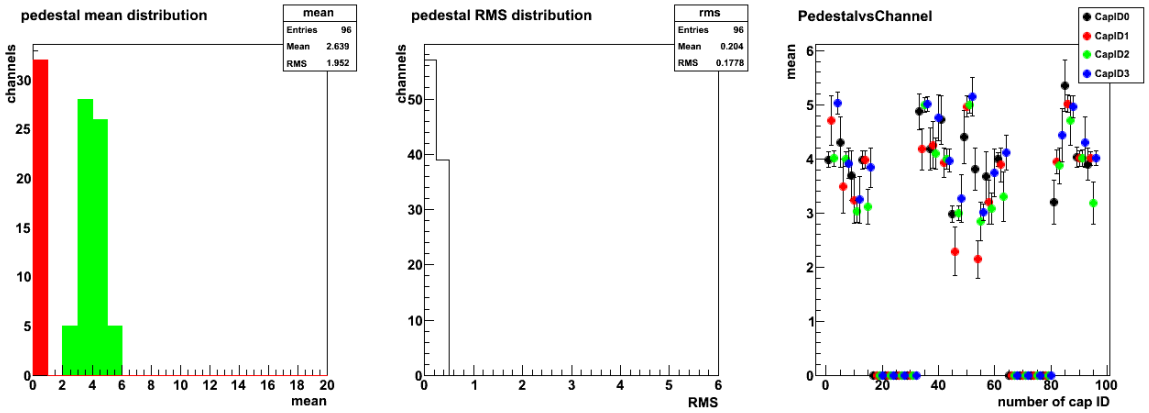

Figure 7.8. Result of a failed Cap ID test due to the Igloo middle link issue. There is an accumulation of 0 ADC on the left histogram. On the right histogram, the middle link pattern can be seen.

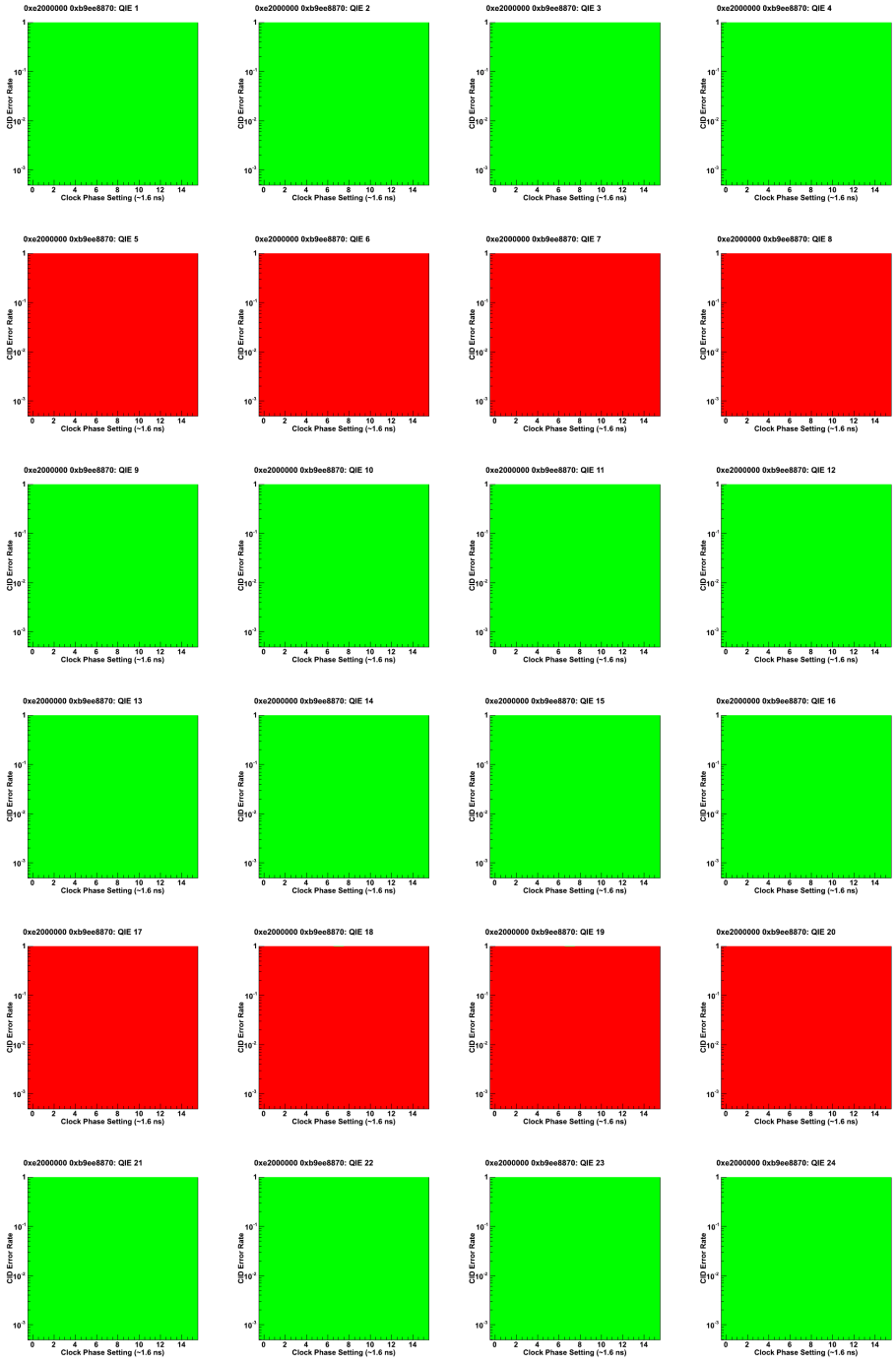

Figure 7.9. Result of a failed pedestal test due to the Igloo middle link issue. Middle link pattern can be seen on the 2nd and 5th rows.

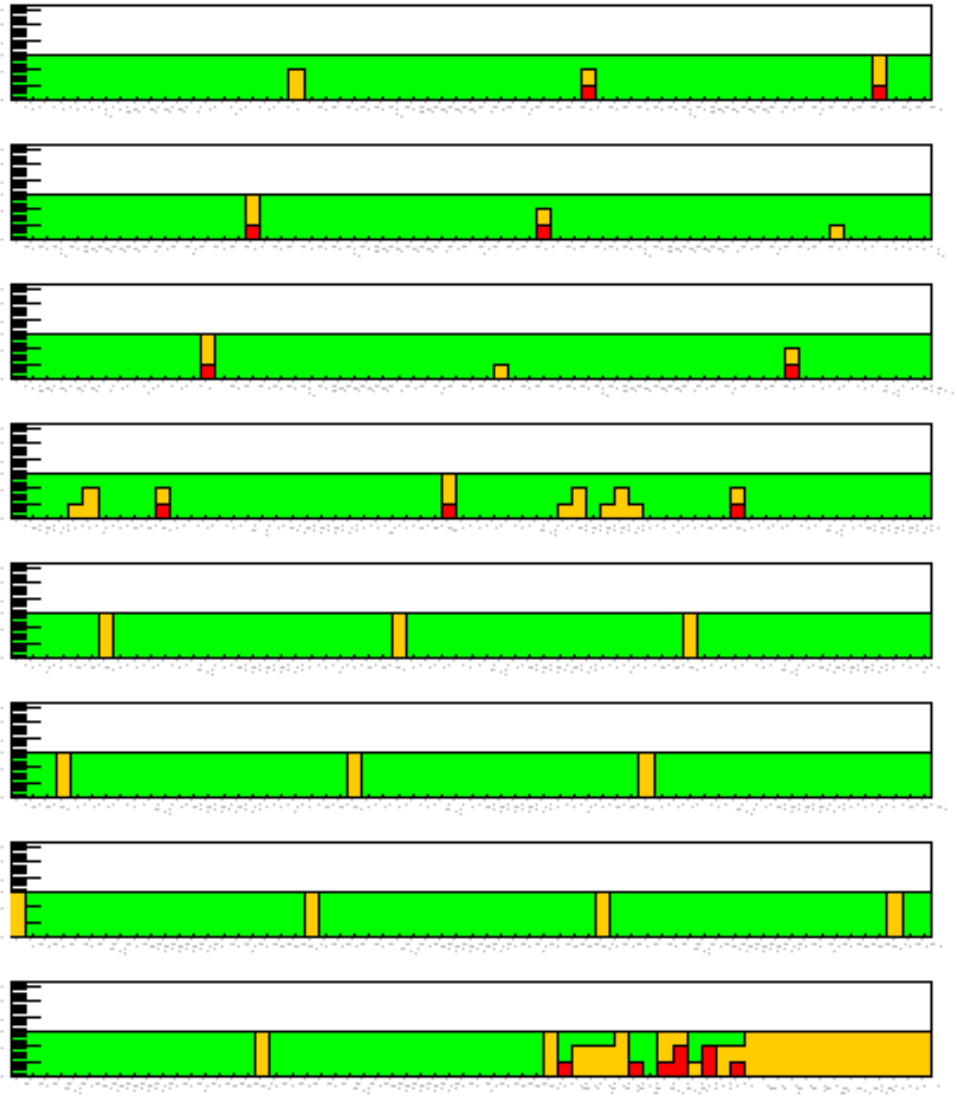

Figure 7.10. Result of a failed register test due to the Bridge FPGA issue. Each bar here represents the test result of a register. Yellow bars in this histogram show the amount of read/write errors and red bars show the amount of read/write mismatches. The problematic registers are the ones that are located in the Igloos. The pattern on the first seven row are caused by the QIE clock phase registers. This register configures the QIE chips, however they are located in the Igloos.

8. CONCLUSION

The main purpose of this study was to assemble, debug and test the new HF-FE cards. Old DAQ system used QIE8 chips and had insufficient amount of channels for the new multi-anode readout scheme. There were two reasons for this upgrade. The first one was to increase the number of channels on the FE DAQ system, so that the new 4-anode PMTs can be connected to the DAQ system as if they were two anode PMTs in order to be able to distinguish the window events from the real events more accurately. The other reason is that the new QIE10s also have a TDC functionality. During the first tests, we have encountered bad Igloo2s with middle link issues, which affected approximately 50% of the cards. We thought that this would be caused by a timing issue on the Igloos due to a firmware instability. This problem did not affect all the cards, because even though the design and the manufacturing process of the chips are the same, they all have slight differences from one another. Thus, some chips tend to be more unstable than the others. A new firmware was developed, which solved the middle link issue completely for most of the cards. There were some register read/write issues on the QIE cards, too. It affected around 20% of the cards. The reason for this was thought to be a firmware instability on the bridge FPGA. A new firmware for the Bridge FPGA solved this problem completely. After all the tests on the 180 QIE cards, we have 4 cards with short circuits between their power planes and 2 cards with data link errors. Also, 3 cards were selected for the radiation tests at the beginning, so these were not tested. So, we have 171 cards that have passed all the tests, which is more than enough for our purposes, since we only need 144 active cards to be installed on the HF.

The plan was to install these cards into the HF by the end of 2015, at the year end technical stop (YETS). However due to the late arrival of the necessary VTTx and the problems with the tests, we realized that they would not be ready for the YETS 2015. The updated plan was to finish the tests with the cards and install them during YETS 2016. In the meantime, it was discovered that the QIE10 chips had a range transition issue. We reported this to Fermilab and the reason for the glitch was identified as an

issue in the QIE10 chips and as a fix, the chips had to be redesigned. Since we have not installed the cards on the detectors, it was decided to replace all the QIE10s on the cards with the corrected ones. This was a significant decision to make, since all the cards would have to be sent to a company for this rework. It will take time to rework all the cards and also due to the rework process, there maybe some damage on them. Right now, the plan is to rework all the cards with the new QIE10s, redo all the tests again and install the cards during YETS 2016. I will continue to work on these cards during Fall 2016.

REFERENCES

1. Evans, L. and P. B. (editors), "LHC Machine", *J. of Instrumentation*, Vol. 2008, No. 3, p. S08001, 2008.

2. Işıldak, B., *Measurement of the differential dijet production cross section in proton-proton collisions at* $\sqrt{s}$ *= 7 TeV.*, unpublished, Boğaziçi University, 2011.

3. CMS Collaboration, "The CMS Experiment at the CERN LHC", *J. of Instrumentation*, Vol. 2008, No. 3, p. S08004, 2008.

4. CMS Collaboration, "Letter of intent: by the CMS Collaboration for a general purpose detector at LHC", Open presentation to the LHCC, 1992, `https://cds.cern.ch/record/290808`, accessed at July 2016.

5. CMS HCAL Collaboration, *The CMS hadron calorimeter project: Technical Design Report*, Tech. Rep. CERN/LHCC 97-31, CMS TDR 2, Geneva, 1997.

6. CMS Collaboration, "Detector Drawings", CMS Collection, 2012, `https://cds.cern.ch/record/1433717`, accessed at July 2016.

7. Brice, M and Virdee, T. S. and Camporesi, T, "Images of CMS HCAL Forward Calorimeter (HF)", CMS Collection, 2008, `https://cds.cern.ch/record/1431489`, accessed at July 2016.

8. CMS HCAL Collaboration, "Design, performance, and calibration of CMS forward calorimeter wedges", *The European Physics Journal C*, Vol. 53, pp. 139–166, 2008.

9. Penzo, A. and Y. Onel, "The CMS-HF quartz fiber calorimeters", *J. of Physics Conference Series*, Vol. 160, p. 012014, 2009.

10. Camporesi, T., "HF fiber stuffing in building 186 at CERN", CMS Collection,

2003, `http://cds.cern.ch/record/43646`, accessed at July 2016.

11. Akgun, U., G. Funk, J. Corso, Z. Jia, D. Southwick, L. Adams, J. Kingyon, E. Tiras, T. Munhollon, E. Troendle, P. Bruecken, V. Khristenko and Y. Onel, "Characterization of 1800 Hamamatsu R7600-M4 PMTs for CMS HF Calorimeter upgrade", *J. of Instrumentation*, Vol. 2014, No. 9, p. T06005, 2014.

12. Akgun, U., E. W. Anderson, A. S. Ayan, E. Gülmez, M. Miller, Y. Onel, I. Schmidt and D. Winn, "Comparison of PMTs From Three Different Manufacturers for the CMS-HF Forward Calorimeter", *IEEE Transactions on Nuclear Science*, Vol. 51, No. 4, pp. 1909–1915, 2004.

13. Akgun, U., A. S. Ayan, G. Aydin, F. Duru, J. Olson and Y. Onel, "Afterpulse timing and rate investigation of three different Hamamatsu Photomultiplier Tubes", *J. of Instrumentation*, Vol. 2008, No. 3, p. T01001, 2008.

14. Gülmez, E., "The CMS Hadron Forward Calorimeter Upgrade during Phase I", *Proceedings of the 14th ICATTP Conference on Astroparticle, Particle, Space Physics, Detectors and Physics Applications*, pp. 568–572, World Scientific, Singapore, 2014.

15. Bilki, B., *Review of scalar meson production at $\sqrt{s}$ = 7 TeV in CMS, U(1)' gauge extensions of the MSSM and calorimetry for future colliders.*, unpublished, University of Iowa, 2011.

16. CMS HCAL Collaboration, *CMS Technical Design Report for the Phase 1 Upgrade of the Hadron Calorimeter*, Tech. Rep. CERN-LHCC-2012-015 CMS-TDR-010, Geneva, 2012.

17. SimPro, *CERN-CMS-PREPROD Kartı Üretim Talimatı*, Tech. Rep. TL-CERN-CMS-PREPROD/10082015/00, İstanbul, 2015.